Double-protected layer with solid–liquid hybrid electrolytes for long-cycle-life lithium batteries

Jiantao Tang[a], Leidanyang Wang[c], Changhao Tian[a], Chunguang Chen[d], Tao Huang[b], Lecai Zeng[c,*] and Aishui Yu[a,b,**]

[a] Department of Chemistry, Collaborative Innovation Center of Chemistry for Energy Materials, Shanghai Key Laboratory of Molecular Catalysis and Innovative Materials, Institute of New Energy, Fudan University, Shanghai 200438, China

[b] Laboratory of Advanced Materials, Fudan University, Shanghai 200438, China

[c] Shanghai Electric Group Co., Ltd. Central Academe, No. 960 Zhongxing Road, Shanghai, 200070, China

[d] Department of Chemistry, College of Science, University of Shanghai for Science and Technology, Shanghai 200093, China.

E-mail: zenglc@shanghai-electric.com (Lecai Zeng*)

E-mail: asyu@fudan.edu.cn (Aishui Yu**)

ABSTRACT : Lithium-ion batteries (LIBs) with liquid electrolytes have problems such as electrolyte leakage, low safety profiles, and low energy density, which limit their further development. However, LIBs with solid electrolytes are safer with better energy and high-temperature performance. Thus, solid electrolytes system batteries have

attracted widespread attention. However, due to the inherent rigidity of the LATP solid electrolyte, there is a high interface impedance at LATP/electrode. In addition, the Ti element in LATP easily reacts with Li metal. Here, we dripped a liquid electrolyte at the LATP/electrode interface (solid-liquid hybrid electrolytes) to reduce its interface impedance. A composite polymer electrolyte (CPE) protective film (containing PVDF, SN and LiTFSI) was then cured in situ at the LATP/Li interface to avoid side reactions of LATP. The discharge specific capacity of the LiFePO$_4$/LATP-12% LE-CPE/Li system is up to 150 mAhg^{-1}, and the capacity retention rate is still 96% after 250 cycles. In addition, the NCM622/PVDF-LATP-12% LE/Li system has an initial reversible capacity of 170 mAhg^{-1}. This study can protect solid electrolytes from lithium metal instability.

1. INTRODUCTION

Efficient and clean green energy is urgently needed. LIBs have received widespread attention because of their light weight, high energy density, and environmental friendliness. They are critical to the energy industry [1-4]. The application of LIBs is continuously expanding, and their performance continues to improve. Mature commercial LIBs use organic liquid electrolytes (LE). Although they have high ionic conductivity, they are prone to interface side reactions with electrodes during battery charging and discharging, especially at high temperatures, leading to

continuous growth of the passivation film [5-7]. However, at low temperatures or under high current charging, lithium can precipitate on the surface of the negative electrode to produce lithium dendrites, which will affect the battery life. At the same time, the low flash point and other defects may cause the battery to burn and explode due to the low thermal stability of the LE. These are key safety issues [8, 9].

Inorganic solid electrolytes have received widespread attention due to their unique characteristics. They are leakproof with low flammability, excellent processing performance, a wide range of electrochemical stability, high safety, high energy density, and excellent thermal stability [10-12]. Among the inorganic electrolytes, sulfide electrolytes, such as $Li_{10}GeP_2S_{12}$ and $Li_{9.54}Si_{1.74}P_{1.44}S_{11.7}Cl_3$ exhibit extremely high ionic conductivity ($>10^{-3}S \cdot cm^{-1}$ at room temperature). However, sulfide is very sensitive to O_2 and H_2O, which limits its application [13-14]. The garnet-type solid electrolyte (lithium ion conductor $Li_5La_3M_2O_{12}$ (M = Nb, Ta) possess high ionic conductivity and excellent mechanical properties, but it easily reacts with H_2O and CO_2 to form Li_2CO_3 on the surface when exposed to the atmosphere causing a significant reduction in electrical conductivity, it also suffers from interface impedances with electrodes [15-16]. LATP solid electrolytes have become critical areas in lithium battery materials in recent years due to their high ion conductivity at room temperature, a wide electrochemical window, easy preparation, and excellent stability [17-20]. However, the LATP solid electrolyte is difficult to use in commercial lithium batteries because of its inherent rigidity, which leads to a very high interfacial resistance at LATP/electrode. There is also unstable contacts between LATP and the Li metal (Ti

will be reduced) [21-23]. The solid–liquid hybrid electrolyte is considered to have the best potential to solve the above mentioned challenges. The LE can wet the interface to minimize solid electrolyte/electrode interface impedances and form a solid–liquid electrolyte interface (SLEI) at the solid electrolyte/Li interface. This in turn prevents the solid electrolyte from being reduced by Li metal [1, 16, 24, 25]. For instance, a solid–liquid hybrid electrolyte was used Li-S and Li-air to suppress the side reaction shuttling effect [26-28]. Xu et al. reduced the interface impedance by adding LE between LLZT and Li metal so that the battery can operate normally [7]. Liu et al. focused on the influence of the LE added on the surface of the LLZTO in terms of interface impedance. In addition, simply adding LE at the cathode/solid electrolyte/anode interface causes the solid electrolyte to will still be reduced by Li metal [16].

In this study, we dripped a dash of functional LE between the LATP and the electrode to reduce its interface impedance. The polymer protective layer is cured in situ at the LATP/Li interface. The composite polymer electrolyte (CPE) protective layer includes polyvinylidene fluoride (PVDF), bistrifluoromethanesulfonimide lithium salt (LiTFSI), and succinonitrile (SN). The role of PVDF is to stabilize lithium metal, and the addition of SN can improve the ionic conductivity and flexibility of PVDF [29-30]. The CPE can effectively protect LATP from the reduction of Li metal. In addition, the LE will also form a SLEI layer between the LATP and Li interface, which can also protect LATP from the reduction of Li metal. Therefore, the resulting double protective layer allows the solid electrolyte to have excellent cycle stability. **Figure 1** shows the
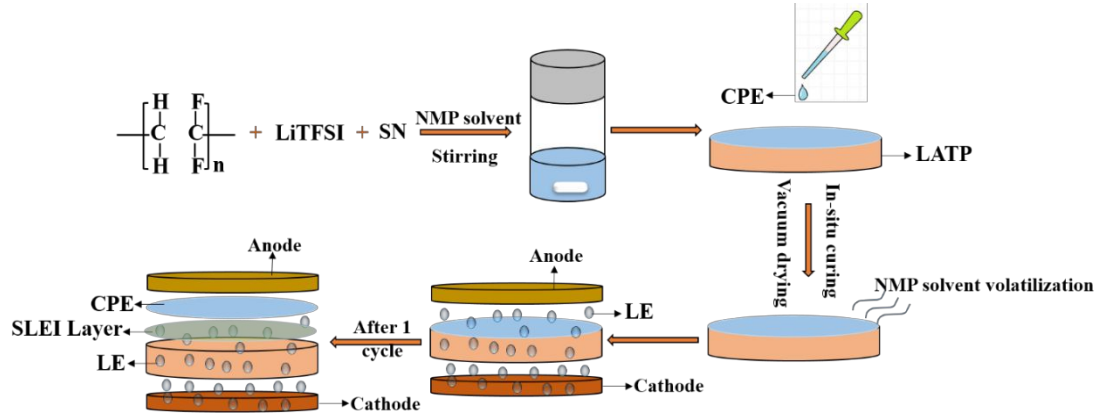
Figure 1. The preparation of CPE and the in situ curing process of CPE on the LATP side and the mechanism of SLEI formation.

preparation of CPE and the process of in situ curing of CPE on the LATP side and the mechanism of SLEI formation.

2. Experimental section

2.1 Preparation of LATP and CPE

LATP were prepared by the previously reported method [31]. The LATP powder was first compressed into pellets. Next, the sheet was placed in a tube furnace for calcination at 900℃ for 6 h. The average thickness of LATP was 0.4 mm.

PVDF (0.45 g), SN (0.5135 g), and LiTFSI (0.135 g) were dissolved in an appropriate amount of N-methylpyrrolidone (NMP) to form a uniform solution (forming CPE). The solution was dripped on LATP and dried in a vacuum drying oven at 90°C for 24 h to achieve in situ curing.

2.2 Characterization of LATP

The morphologies of LATP and positive electrode were evaluated by scanning

electron microscopy (SEM, S-4800) and high resolution tunneling electron microscope (HRTEM). The chemical states of the LATP were characterized by X-ray photoelectron spectroscopy (XPS, PHI 5000&PHI 5300). The structures of LATP were analyzed by X-ray diffractometry (XRD, SMART APEX II, BRUKER) and selected area electron diffraction (SAED). In addition, the CPE cured in situ on one side of LATP was removed when characterizing the LATP after cycling.

2.3 Cell Assembly

The $LiFePO_4$ (LFP) and $LiNi_{0.6}Mn_{0.2}Co_{0.2}O_2$ (NCM) cathode were prepared by mixing LFP/NCM (80 wt%), super P (10 wt%)and PVDF (10 wt%) in NMP and cast on Al foil, This was then dried at 80°C under vacuum for 12 h. The mass loading of LFP/NCM622 is 2 mg/cm^2. The LE contained 0.575M LiTFSI and 0.575M $LiPF_6$ were dissolved in ethylene carbonate (EC), dimethyl carbonate (DMC), and ethyl methyl carbonate (EMC) (in 1:1:1vol%) with 5 vol% trimethyl phosphate (TMP), 5 vol% fluoroethylene carbonate (FEC), and 1 vol% 1,3-propane sultone (PS). The LE was added to the positive electrode/LATP-CPE/Li interface, where the amount of LE dripped was the volume ratio of LE to LATP of 8%, 12%, and 15%, and marked as LATP- 8% LE-CPE (LE-6 μL), LATP-12% LE-CPE (LE-9.1 μL), and LATP-15% LE-CPE (LE- 11.3 μL), respectively.

2.4 Electrochemical measurements

Electrochemical impedance spectroscopy (EIS) of solid–liquid hybrid electrolyte cells tests was conducted between 1 MHz and 0.1 Hz on a Autolab. Linear sweep

voltammetry (LSV) was performed from 0 V to 6 V at 0.1 mV s^{-1}. Electrochemical
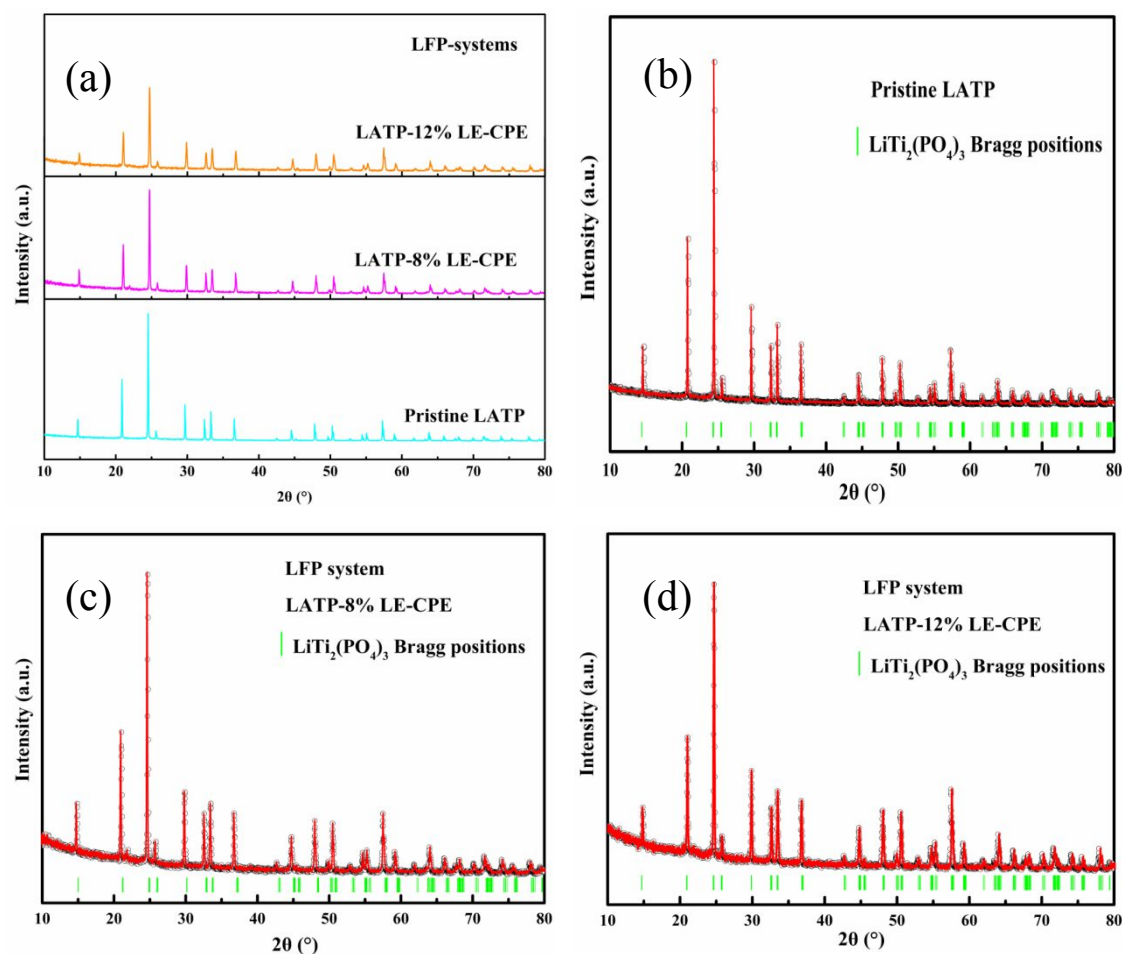

Figure 2. XRD patterns (a) and the Rietveld refinements of pristine LATP and LATP-x% LE-CPE materials after 100 cycles, (b) pristine LATP, (c) x = 8, and (d) x = 12.

analysis used a Wuhan Land battery (at 25℃).

3. Results and discussion

3.1 Structure and Morphology characteristics

We used XRD to detect the structural changes of the original LATP, LATP-8% LE-CPE and LATP-12% LE-CPE after 100 cycles. **Figure 2** shows the LATP sample structure indicating a typical NASICON-type structure [32-33]. In both LFP and

NCM622 cathode material systems, the LATP in LATP-8% LE-CPE and LATP-12%-CPE still maintains its original structure after 250 cycles. We next refined the XRD of
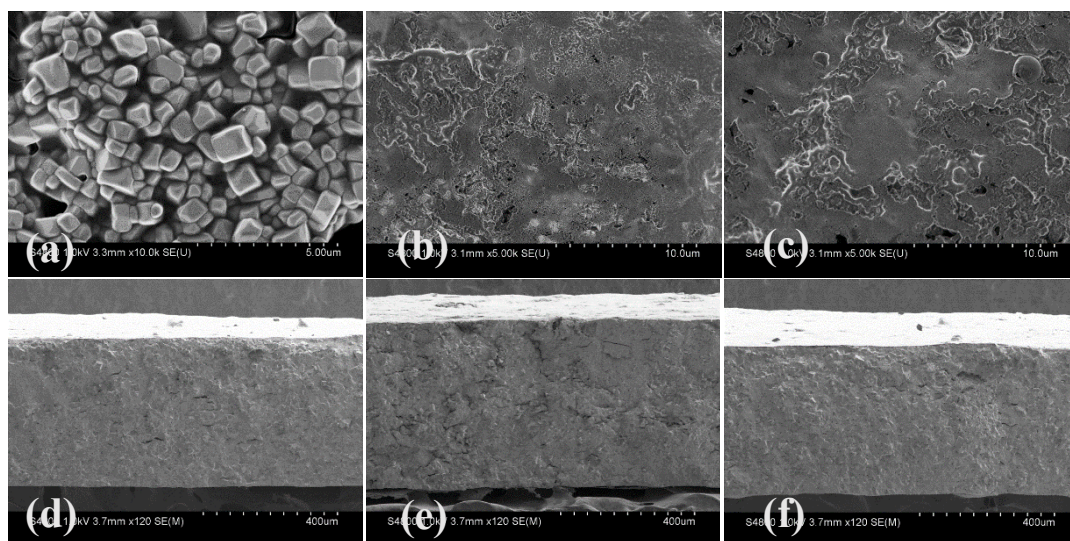

Figure 3. Cross-section SEM images of (a) pristine LATP and (b) LATP-8% LE-CPE, and (c) LATP-12% LE-CPE materials after 100 cycles; SEM images of d) pristine LATP and (e) LATP-8% LE-CPE, and (f) LATP-12% LE-CPE materials after 100 cycles (top view).

the LATP to further confirm whether the second phase (the phase in which LATP is reduced by Li) appears in the two cathode material systems. The refined results are shown in Table S1 and S2. No second phase has been produced, and the results of various parameters show that it still maintains the NASICON-type structure [31]. The results above show that LATP is protected by a SLEI and CPE double protection layer, and thus LATP is not reduced.

Figure 3 presents the SEM images of pristine LATP, LATP-8% LE-CPE, and LATP-12% LE-CPE sample after 100 cycles. The pristine LATP clearly shows uniform particles (**Figure 3a**). However, LATP-8%LE-CPE and LATP-12%LE-CPE form a

layer similar to SLEI on the surface that can protect LATP from being reduced by Li

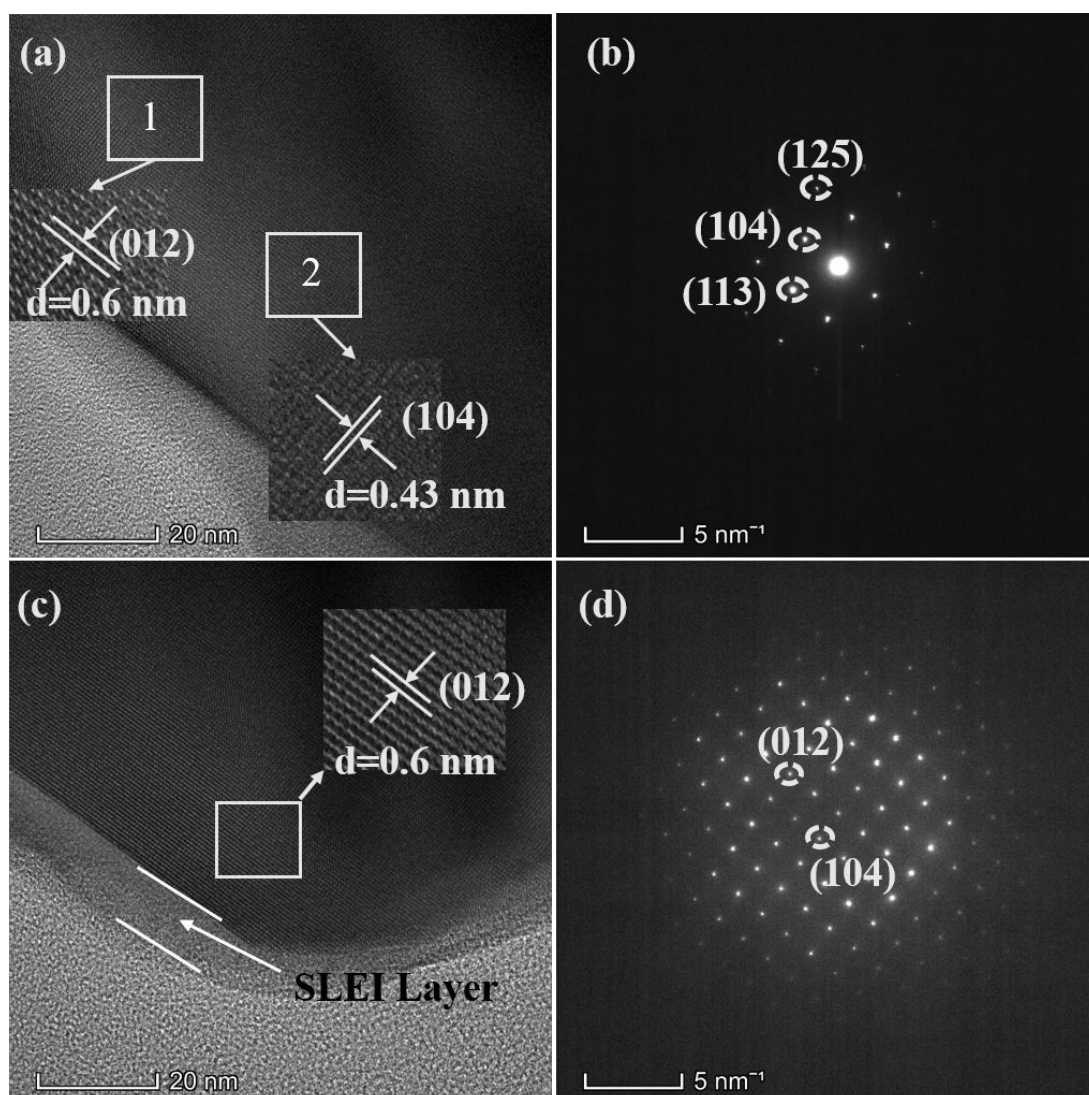metal. In addition, the LE is exhausted after LATP-8%LE-CPE is circulated for 80

Figure 4. HRTEM images of (a) pristine LATP and (c) LATP-12% LE-CPE materials

after 100 cycles, and corresponding SAED (b) of pristine LATP and (d) LATP-12%

LE-CPE materials after 100 cycles.

cycles. However, there is no crack in LATP (**Figure 3b and e**) indicating that LATP

has not been reduced. This is because that although the electrolyte has been consumed,

the SLEI protective layer can no longer be generated. However, there is still a CPE

protective layer in place LATP/Li interface. Consequently, no reduction products enter the interior of the LATP particles, and there will be no drastic changes in internal stress. Accordingly, the LATP will not crack even if the LE of the LATP-8% LE-CPE sample is consumed. This result is different from what we previously reported [31].

The crystal structure information of pristine LATP, LATP-8% LE-CPE, and LATP-12% LE-CPE after 100 cycles were further tested by HRTEM and SAED. **Figure 4a** displays a typical HRTEM image of the pristine LATP lattice. The lattice spacing of region 1 and region 2 are 0.6 nm and 0.43 nm, which corresponds to the (012) and (104) crystal planes. These data suggest that the pristine LATP has a NASICON-type structure. The (125), (104), and (113) planes in SAED also prove this. **Figure S1a and b** shows the crystal structure of the LATP-8% LE-CPE sample, The LATP-8% LE-CPE sample shows a lattice fringe distance of 0.35 nm, which corresponds to the (202) plane of SAED. This phenomenon is in contrast to the literature (LATP is reduced to amorphous phase after the electrolyte is consumed) [10, 31], However, the generation of SLEI was still detected (perhaps the SLEI generated before the liquid electrolyte was completely consumed). The results suggest that CPE cured in situ between LATP and Li metal can effectively avoid side reactions of LATP (even if there is no LE to form SLEI at the LATP/Li interface). The internal surface structure of the LATP-12%LE-CPE sample is consistent with that of pristine LATP and LATP-8%LE-CPE. However, a similar SLEI layer was detected on the outer surface and may contain LiF and Li_2CO_3 (**Figure 4c and d**) [7, 10].

3.2 XPS analysis

The XPS of pristine LATP, LATP-8% LE-CPE and LATP-12% LE-CPE after 100

cycles was used to identify the chemical state and components of LATP solid
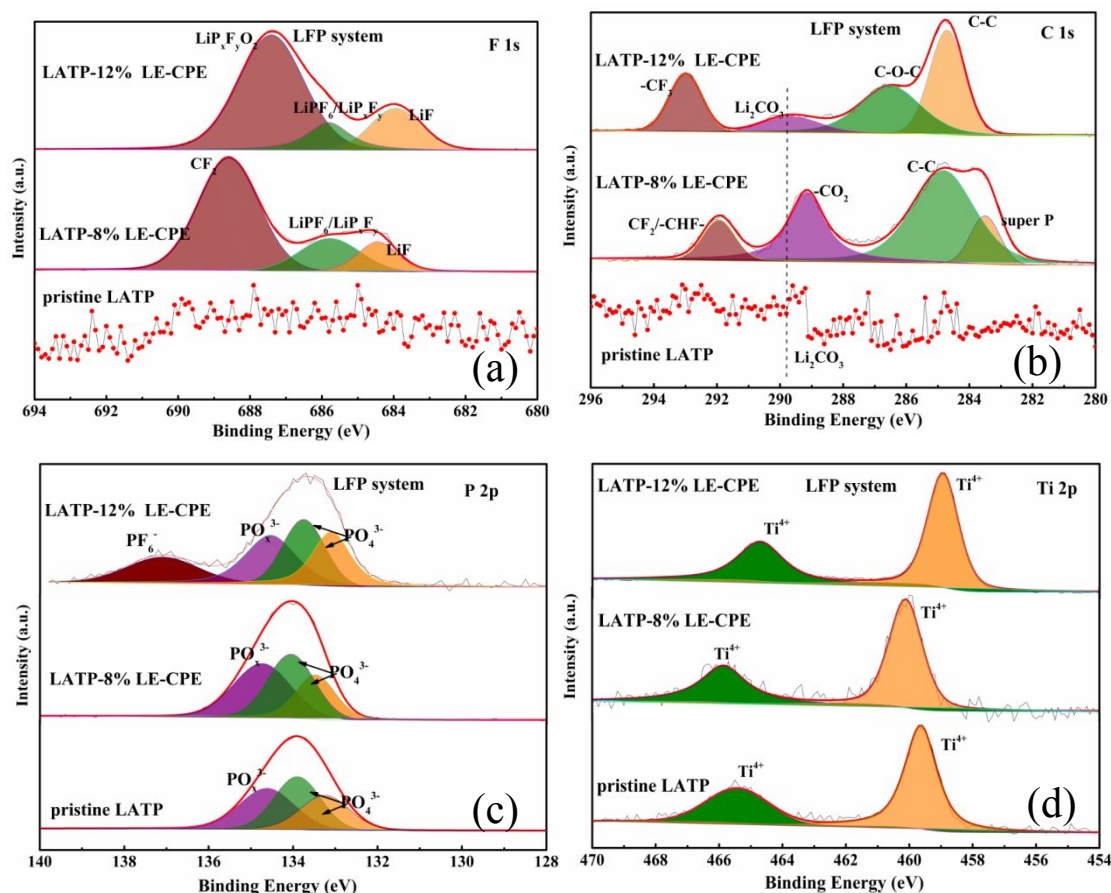

Figure 5. LFP system: XPS spectra of (a) fluorine, (b), carbon (c) phosphorus and (d)

titanium in the pristine LATP and LATP-x% LE-CPE after 100 cycles (x = 8, 12).

electrolyte interface (**Figure 5**). In the LFP system, an F1s spectrum of the pristine

LATP shows that no F peak is detected. However, there are three peaks for the LE

addition 8% and 12% after 100 cycles. Three peaks located around 684.4, 685.8, 287.9,

and 688.6/687.4 eV could belong to LiF, LiP_xF_y and $CF_2/LiP_xF_yO_2$, respectively. The

component LiF of SLEI is produced due to the decomposition of FEC and $LiPF_6$ in LE.

The residual $LiP_xF_yO_2$ on the LATP is caused by the decomposition of $LiPF_6$. In **Figure**

5b, unlike the pristine LATP solid electrolyte, three peaks appear in LATP-8% LE-CPE

and LATP-12% LE-CPE, which are attributed to super P (around 283.5 eV), C-C (around 284.75 eV), C-O-C (around 286.51 eV), $-CO_2$ (around 289.1 eV), Li_2CO_3
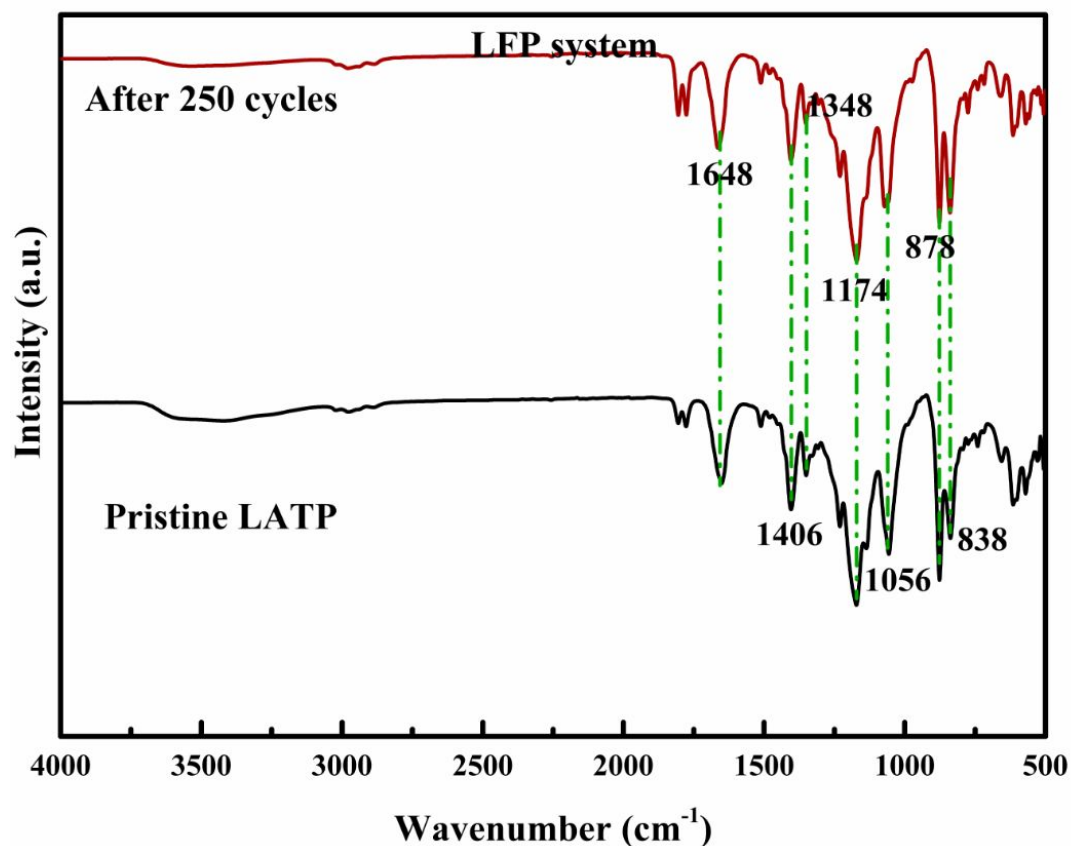

Figure 6. FT-IR spectra images of CPE before and after 250 cycles.

(around 289.7 eV), CF_2/-CHF- (around 291.9 eV), and $-CF_3$ (around 293 eV). **Figure 5c** shows two peaks at 133.2 and 133.9 eV associated with PO_4^{3-}. The peak at 134.6 eV is associated with PO_x^{3-}, and the binding energies of 137.1 eV are assigned to PF_6^{-}, which may be because the $LiPF_6$ salt is not entirely removed by DMC washing [37]. **Figure 5d** demonstrates that all Ti 2p are located near 459.7 and 465.6 eV, suggesting that the Ti-ion exists at +4, which means that the protective layer of SLEI and PVDF effectively prevent the reduction of LATP by Li metal, thus improving the electrochemical performance of the battery [38]. **Figure S2** shows the state and

composition of carbon, fluorine, phosphorus and titanium of PVDF-LATP-8% LE in the NCM622 system. The state and composition are very similar to those of LFP system. A SLEI protective layer containing LiF and Li_2CO_3 is also produced on the surface of the solid electrolyte. Consequently, the PVDF and SLEI layers double-protect the LATP, which further improves the battery's electrochemical performance.

3.3 FTIR analysis

The changes of functional group peaks before and after the CPE sample cycle were recorded by FTIR spectroscopy (**Figure 6**). We assigned the vibrational absorption peaks at 838 and 878 cm^{-1} to the PVDF polymer. The peaks at 1174 and 1406 cm^{-1} are characteristic signatures of CF_3 and CF, respectively. Peaks at 1056 and 1348 cm^{-1} are attributed to the S–N–S of SN and C–SO_2–N wagging and stretching, respectively. The sharp peaks at 1648 cm^{-1} represent the C=O stretching mode. This phenomenon is due to the interaction between the PVDF framework and LiTFSI [17, 35]. The appearance of the peaks above suggests that the film has a PVDF-LiTFSI-SN structure. The analysis results indicate that the structure of CPE remains stable before and after the cycle.

3.4 Battery electrochemical performance

The interfacial stability window of the LATP is related to whether it nicely matches the positive and negative electrode materials. Therefore, we used linear scanning to detect the electrochemical stability window of LATP-12% LE-CPE electrolyte (**Figure S3**). Here, Li metal represents the counter electrode and the

reference electrode, and SS is the working electrode. The solid electrolyte has no oxidation current in the voltage range of 0–6 V, indicating that it is stable from 0 to 6 V to meet the application
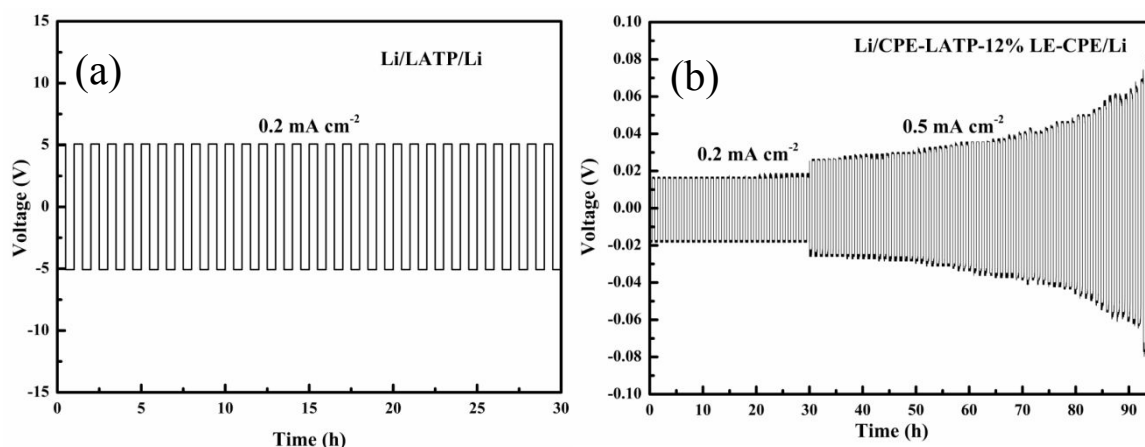

Figure 7. Galvanostatic cycling curves of (a) Li/LATP/Li and (b) Li/LATP-12% LE-CPE/Li cells.

requirements of LIBs [34].

The influence of the LE and CPE protective layer on the electrochemical performance of the LATP was tested by cycling at 0.2 mA cm^{-1} and 0.5 mA cm^{-1}. The initial voltage polarization of Li/LATP/Li is very high (**Figure 7a**), and it increases rapidly as the cycle progresses, which reflects the deteriorating interface. In sharp contrast, the addition of LE and the LATP (cured in situ) of the CPE protective layer endows the Li/Li symmetric battery stable cycling for 95 h. The test of the lithium symmetric battery at a higher current density (0.5 mA cm^{-2}) further proved the stability of the interface between LATP and Li. **Figure 7b** shows that the overpotential does not increase significantly after 95 h. The addition of LE and the in-situ curing of the CPE protective layer also played an important role in the stability of the Li/LATP interface.

To confirm the influence of LE and the CPE protective layer on LATP impedance, EIS tests of Li/LATP-12% LE-CPE/Li, and Li/LATP/Li cells were performed. The Nyquist plots of Li/Li symmetric cells are given in **Figure 8**. The EIS plots can be fitted into two well-separated semicircles. The high–frequency region is the bulk resistance
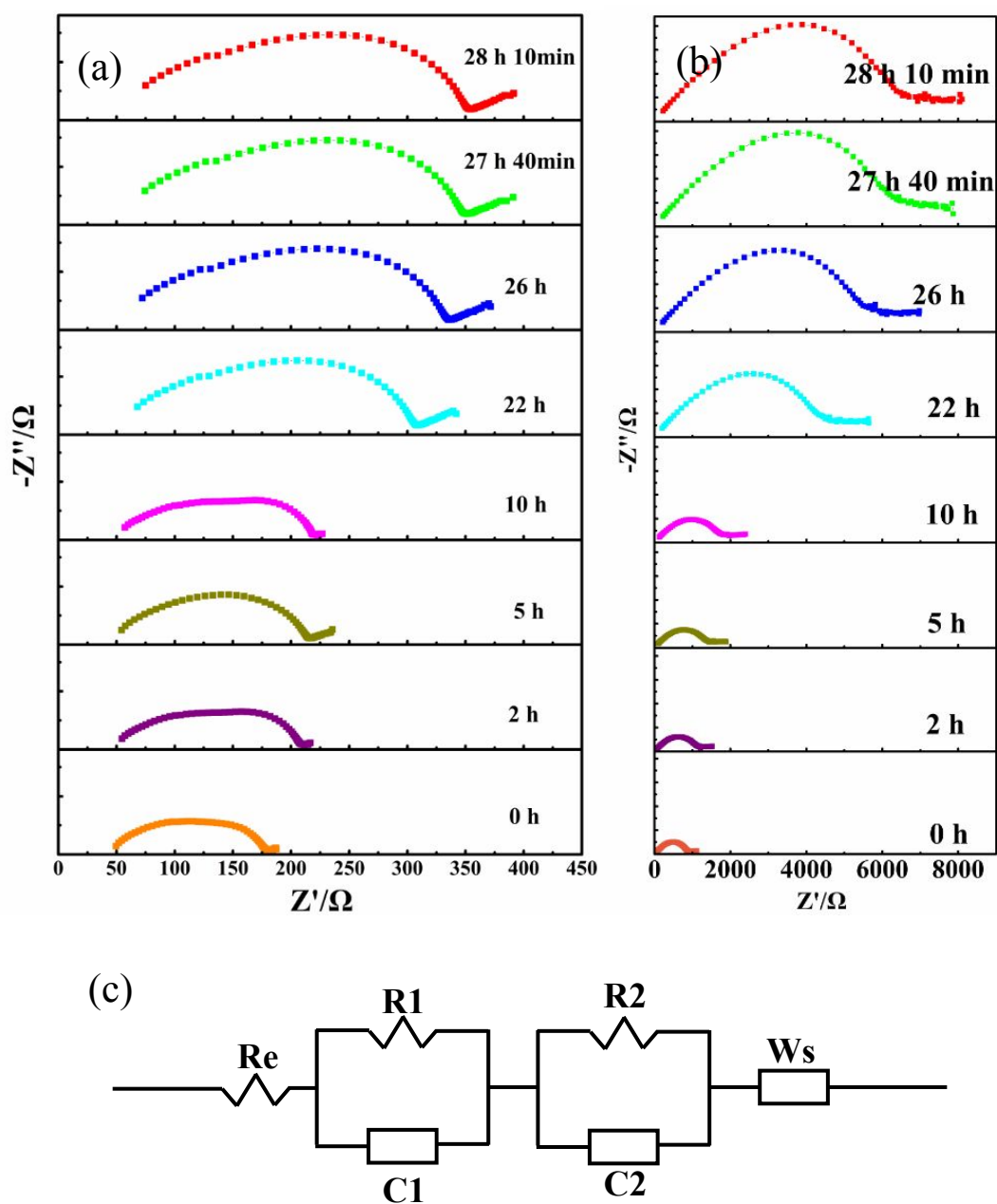

Figure 8. EIS of (a) Li/LATP-12% LE-CPE/Li and (b) Li/LATP/Li symmetric cells, (c) the equivalent circuit.

of the solid electrolyte. The mid–high frequency region corresponds to the grain boundary resistance of the solid electrolyte. The resistance in the low frequency region is attributed to the charge transfer resistance, and the parallel constant phase element (C) corresponds to the interface capacitance at LATP-CPE/Li [1, 36]. Compared to the pristine LATP, LATP with a LE and CPE protective layer has little change in overall impedance over time (increased from 125 Ω to 275 Ω). However, Li/LATP/Li system battery has an initial overall impedance that is very high (about 1000 Ω), and its impedance increases to 7000 Ω after 28 h 10 min. We disassembled Li/LATP-12% LE-CPE/Li, and Li/LATP/Li symmetric cells, respectively (**Figure S4**). The samples with LE and the in
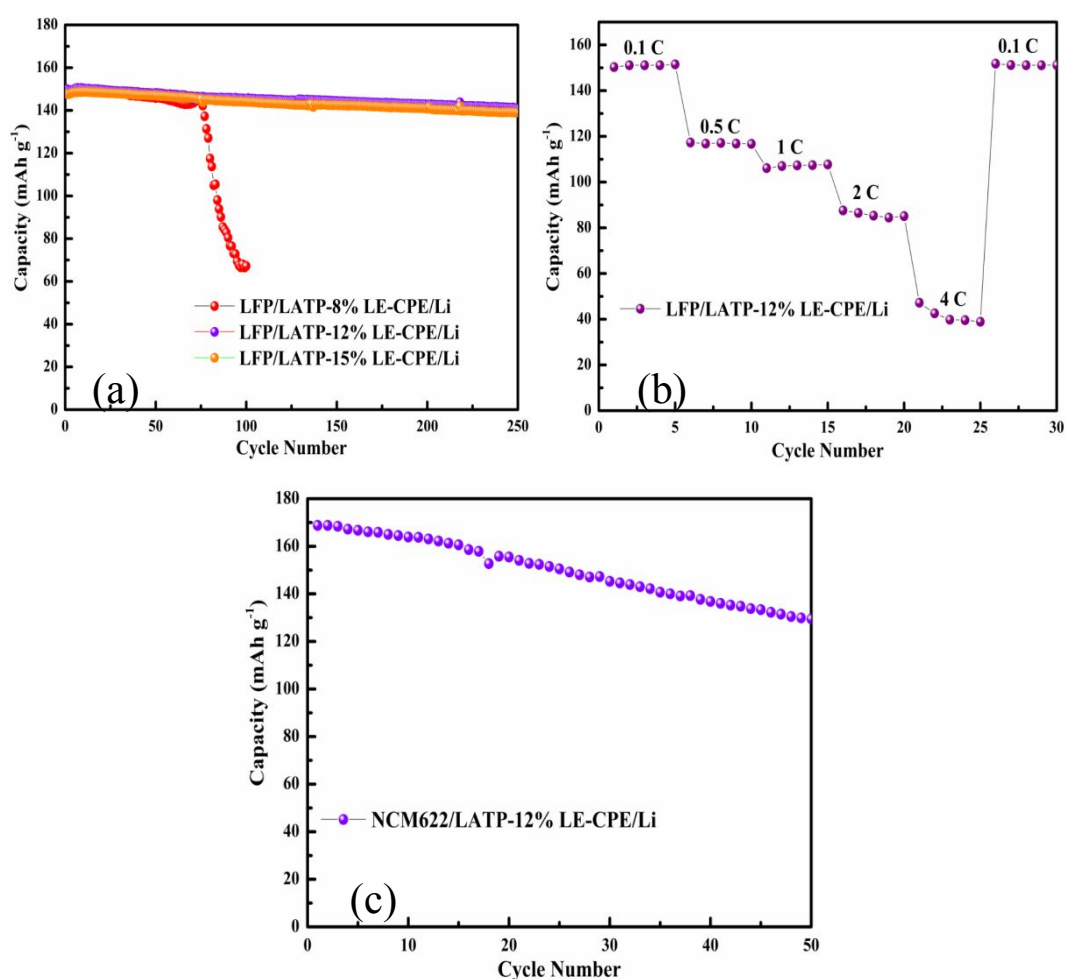
Figure 9. (a) Cycle performances and (b) rate capabilities for LFP/LATP-12% LE-CPE/Li. (c) Cycle performances for NCM622/LATP-12% LE-CPE/Li.

situ cured CPE layer of LATP hardly reduced, but the pristine LATP reduced dramatically (becoming almost brittle), which is consistent with our previous report [31].

The long-term cycling performances of LFP/LATP-x% LE-CPE/Li (x =8, 12, 15) were evaluated at 0.1 C from 2.5–4.0 V. (**Figure 9a**). The initial reversible capacity of the LFP system battery is 150 mAh g^{-1} when 8% LE is added to LATP-CPE, but the battery starts to fail after 80 cycles of cycling. This is because LE is almost consumed during the cycle, which causes the LATP-CPE/electrode interface impedance to continue to increase, eventually, the battery fails. However, the LFP battery assembled with LATP-12% LE-CPE and LATP-15% LE-CPE samples show excellent initial discharge specific capacity (150 mAh g^{-1}) and cycle performance. Their capacity after 250 cycles is still over 96%. Both the discharge capacity and the capacity retention rate are better than those previously reported in the literature [16, 32, 38], because the LE generates SLEI at the side of LATP relative to Li, thereby protecting LATP from being reduced. Additionally, the CPE protective layer is cured in situ on LATP giving LATP double protection, Finally, there is always a LE in the battery to connect the interface at cathode/solid electrolyte/anode (the interface impedance is small), accordingly, the lithium ion has a continuous transmission channel. **Figure 9b** shows the rate capabilities of LFP/LATP-12% LE-CPE/Li as the current density increases from 0.1 C

to 4 C and returns to 0.1 C. The LFP/LATP-12% LE-CPE/Li delivers a mean discharge capacity of 103.94, 71.24, 52.79, 35.32 and 13.55 mA h g^{-1} at 0.1 C, 0.5 C, 1 C, 2 C and 4 C, respectively. When this rate returns to 0.1 C, the discharge capacity of the LFP/LATP-12% LE-CPE/Li can recover to 150 mAh g^{-1}. The low discharge specific capacity of the LFP/LATP-12% LE-CPE/Li battery at a high rate may be due to the relatively high interfacial impedance. The NCM622/LATP-12% LE-CPE/Li system battery was next assembled to increase the energy density of the battery, The initial discharge specific capacity is 170 mA h g^{-1} (**Figure 9c**), and the capacity retention rate is 80% after 50 cycles. The reason for the rapid capacity decay will be explained below.

Next, to understand the capacity decay of NCM622 system batteries, NCM622/LATP-12% LE-CPE/Li half-cells were prepared and the EIS were tested.
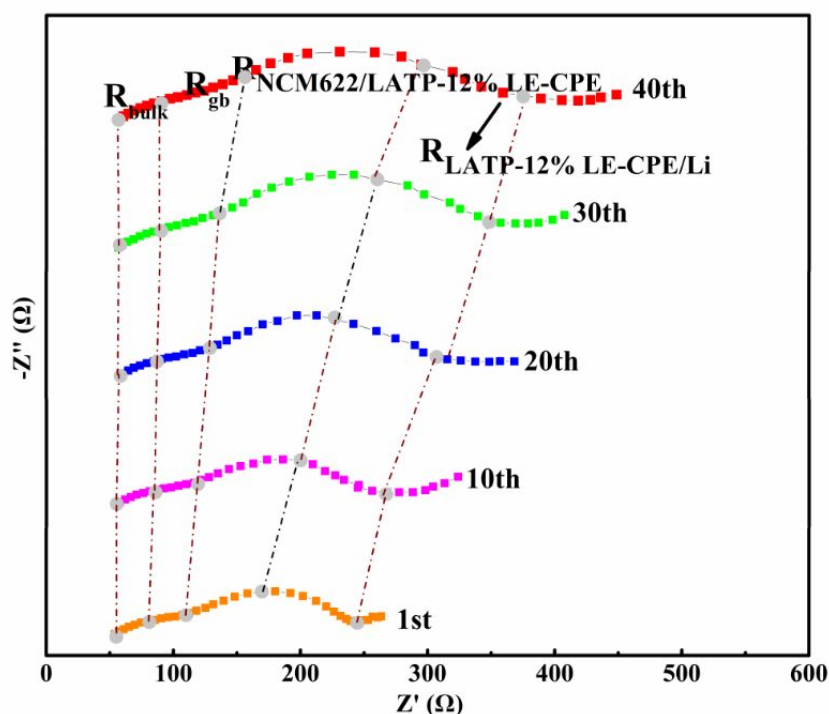

Figure. 10. EIS of NCM622/LATP-12% LE-CPE/Li system cell at different cycles.

Figure 10 shows the EIS of the half-cell after the 1st, 10th, 20th, 30th, and 40th cycles.

The high-frequency region is related to the volume resistance, the frequency region of 1.23 kHz–2.85 Hz can be assigned to the grain boundary resistance, and the low-frequency region corresponds to the interface resistance of solid electrolyte/NCM622 and solid electrolyte/Li [39, 40]. Each impedance increases as the cycle progresses, and the LATP-12% LE-CPE/NCM622 interface impedance increases more obviously. The increase in the solid electrolyte/positive electrode interface impedance is the main reason for the capacity decline of NCM622 positive electrode material system. Obviously, long-term cycling performance can be achieved in solid-state batteries when LATP-12% LE-CPE is employed with NCM622 cathode material, if the interface is stable during cycling.

4. CONCLUSIONS

A protective layer containing PVDF, SN, and LiTFSI was successfully cured in situ on LATP. The interface impedance is significantly reduced after dripping the LE at the LATP/electrode interface. A SLEI protective layer is generated at interface of LATP/Li. Therefore, there is a double protective layer at the LATP/Li interface to avoid side reactions of LATP. The test results of EIS show that the interface resistance of the Li/LATP-12%LE-CPE/Li symmetric battery is much lower than that of the Li/LATP/Li. Moreover, the interface resistance of the Li/LATP-12% LE-CPE/Li battery increases only slightly after 28 h 10 min of cycling. However, the Li/LATP/Li system cell increased from 1000 Ω to 7000 Ω. The XPS results show that Ti^{4+} is not reduced to Ti^{3+} after a SLEI and CPE protective film is cured in situ on the surface of LATP. The discharge specific capacity of the LFP/LATP-12% LE-CPE/Li system battery is as high

as 150 mAh g^{-1}, and its capacity retention rate is 96% after 250 cycles. This system battery has an excellent discharge specific capacity and capacity retention rate due to the double protective layer of SLEI and CPE. In addition, the initial reversible capacity of the NCM622/LATP-12% LE-CPE/Li system battery is 170 mAh g^{-1}, but the capacity retention rate is relatively low (the capacity retention rate is 80% after 50 cycles). This approach can be can be used in other oxide solid electrolytes, to reduce the interface impedance and protect the solid electrolyte from being reduced by Li metal.

ASSOCIATED CONTENT

Supporting Information

HRTEM images of LATP-8% LE-CPE materials and corresponding SAED. NCM622 system: XPS spectra of LATP-12% LE-CPE sample. LSV curves of SS/LATP-12% LE-CPE/Li. Photograph of an as-prepared LATP sample, pristine LATP and LATP-12% LE-CPE samples after 28 h 10 min of EIS testing. The crystallographic parameters of LATP samples.

AUTHOR INFORMATION

Corresponding Authors

Lecai Zeng – Shanghai Electric Group Co., Ltd. Central Academe, No. 960 Zhongxing Road, Shanghai, 200070, China; E-mail: zenglc@shanghai-electric.com

Aishui Yu – Department of Chemistry, Shanghai Key Labor- atory of Molecular Catalysis and Innovative Materials, Collaborative Innovation Center of Chemistry for

Energy Materials, Fudan University, Shanghai 200438, China; Laboratory of Advanced

Materials, Fudan University, Shanghai 200438, China;

orcid.org: 0000-0002-8135-5123;

E-mail: asyu@fudan.edu.cn

Authors

Jiantao Tang – Department of Chemistry, Shanghai Key Laboratory of Molecular

Catalysis and Innovative Materials, Collaborative Innovation Center of Chemistry for

Energy Materials, Fudan University, Shanghai 200438, China

Leidanyang Wang – Shanghai Electric Group Co., Ltd. Central Academe, No. 960

Zhongxing Road, Shanghai, 200070, China

Changhao Tian – Department of Chemistry, Shanghai Key Laboratory of Molecular

Catalysis and Innovative Materials, Collaborative Innovation Center of Chemistry for

Energy Materials, Fudan University, Shanghai 200438, China

Chunguang Chen – Department of Chemistry, School of Materials and Chemistry,

University of Shanghai for Science and Technology, Shanghai 200093, China.

Tao Huang – Laboratory of Advanced Materials, Fudan University, Shanghai 200438,

China

ACKNOWLEDGMENT

REFERENCES

(1) Wang, C.; Sun, Q.; Liu, Y.; Zhao, Y.; Li, X.; Lin, X.; Banis, M. N.; Li, M.; Li, W.; Adair, K. R.; Wang, D.; Liang, J.; Li, R.; Zhang, L.; Yang, R.; Lu, S.; Sun, X. Boosting the performance of lithium batteries with solid-liquid hybrid electrolytes: Interfacial properties and effects of liquid electrolytes. *Nano Energy* **2018**, *48*, 35-43;.

(2) Siyal, S. H.; Li, M.; Li, H.; Lan, J.-L.; Yu, Y.; Yang, X. Ultraviolet irradiated PEO/LATP composite gel polymer electrolytes for lithium-metallic batteries (LMBs). *Appl. Surf. Sci.* **2019**, *494*, 1119-1126.

(3) Lu, Y.; Zhang, X.; Xue, C.; Xin, C.; Li, M.; Nan, C.-w.; Shen, Y. Three-dimensional structured asymmetric electrolytes for high interface stability and fast Li-ion transport in solid-state Li-metal batteries. *Mater. Today Ene.* **2020**, *18*, 100522.

(4) Yue, H.; Li, J.; Wang, Q.; Li, C.; Zhang, J.; Li, Q.; Li, X.; Zhang, H.; Yang, S. Sandwich-Like Poly(propylene carbonate)-Based Electrolyte for Ambient-Temperature Solid-State Lithium Ion Batteries. *ACS Sustain. Chem. Eng.* **2017**, *6*, 268-274.

(5) Sun, Y. Y.; Wang, Y. Y.; Li, G. R.; Liu, S.; Gao, X. P. Metalophilic Gel Polymer Electrolyte for in Situ Tailoring Cathode/Electrolyte Interface of High-Nickel Oxide Cathodes in Quasi-Solid-State Li-Ion Batteries. *ACS Appl. Mater. Interfaces* **2019**, *11*, 14830-14839.

(6) Zhang, W.; Nie, J.; Li, F.; Wang, Z. L.; Sun, C. A durable and safe solid-state lithium battery with a hybrid electrolyte membrane. *Nano Energy* **2018**, *45*, 413-419.

(7) Liu, J.; Gao, X.; Hartley, G. O.; Rees, G. J.; Gong, C.; Richter, F. H.; Janek, J.; Xia, Y.; Robertson, A. W.; Johnson, L. R.; Bruce, P. G. The Interface between $Li_{6.5}La_3Zr_{1.5}Ta_{0.5}O_{12}$ and Liquid Electrolyte. *Joule* **2020**, *4*, 101-108.

(8) Yu, X.; Manthiram, A. A review of composite polymer-ceramic electrolytes for lithium batteries. *Energy Storage Mater.* **2021**, *34*, 282-300.

(9) Tolganbek, N.; Yerkinbekova, Y.; Khairullin, A.; Bakenov, Z.; Kanamura, K.; Mentbayeva, A. Enhancing purity and ionic conductivity of NASICON-typed $Li_{1.3}Al_{0.3}Ti_{1.7}(PO_4)_3$ solid electrolyte. *Ceram. Int.* **2021**, *47*, 18188-18195.

(10) Cheng, Q.; Li, A.; Li, N.; Li, S.; Zangiabadi, A.; Li, T.-D.; Huang, W.; Li, A. C.; Jin, T.; Song, Q.; Xu, W.; Ni, N.; Zhai, H.; Dontigny, M.; Zaghib, K.; Chuan, X.; Su, D.; Yan, K.; Yang, Y. Stabilizing Solid Electrolyte-Anode Interface in Li-Metal Batteries by Boron Nitride-Based Nanocomposite Coating. *Joule* **2019**, *3*, 1510-1522.

(11) Kasemchainan, J.; Zekoll, S.; Spencer Jolly, D.; Ning, Z.; Hartley, G. O.; Marrow, J.; Bruce, P. G. Critical stripping current leads to dendrite formation on plating in lithium anode solid electrolyte cells. *Nat. Mater.* **2019**, *18*, 1105-1111.

(12) DeWees, R.; Wang, H. Synthesis and Properties of NaSICON-type LATP and LAGP Solid Electrolytes. *ChemSusChem* **2019**, *12*, 3713-3725.

(13) Adeli, P.; Bazak, J. D.; Park, K. H.; Kochetkov, I.; Huq, A.; Goward, G. R.; Nazar, L. F. Boosting Solid-State Diffusivity and Conductivity in Lithium Superionic Argyrodites by Halide Substitution. *Angew. Chem. Int. Ed. Engl.* **2019**, *58*, 8681-8686.

(14) Kraft, M. A.; Ohno, S.; Zinkevich, T.; Koerver, R.; Culver, S. P.; Fuchs, T.; Senyshyn, A.; Indris, S.; Morgan, B. J.; Zeier, W. G. Inducing High Ionic Conductivity

in the Lithium Superionic Argyrodites $Li_{6+x}P_{1-x}Ge_xS_5I$ for All-Solid-State Batteries. *J. Am. Chem. Soc.* **2018**, *140*, 16330-16339.

(15) Seo, J.-H.; Nakaya, H.; Takeuchi, Y.; Fan, Z.; Hikosaka, H.; Rajagopalan, R.; Gomez, E. D.; Iwasaki, M.; Randall, C. A. Broad temperature dependence, high conductivity, and structure-property relations of cold sintering of LLZO-based composite electrolytes. *J. Eur. Ceram. Soc*. **2020**, *40*, 6241-6248.

(16) Xu, B.; Duan, H.; Liu, H.; Wang, C. A.; Zhong, S. Stabilization of Garnet/Liquid Electrolyte Interface Using Superbase Additives for Hybrid Li Batteries. *ACS Appl. Mater. Interfaces* **2017**, *9*, 21077-21082.

(17) Shi, X.; Ma, N.; Wu, Y.; Lu, Y.; Xiao, Q.; Li, Z.; Lei, G. Fabrication and electrochemical properties of LATP/PVDF composite electrolytes for rechargeable lithium-ion battery. *Solid State Ionics* **2018**, *325*, 112-119.

(18) Gai, J.; Ma, F.; Zhang, Z.; Sun, D.; Jin, Y.; Guo, Y.; Kim, W. Flexible Organic–Inorganic Composite Solid Electrolyte with Asymmetric Structure for Room Temperature Solid-State Li-Ion Batteries. *ACS Sustain. Chem. Eng.* **2019**, *7*, 15896-15903.

(19) Zhou, Q.; Li, Q.; Liu, S.; Yin, X.; Huang, B.; Sheng, M. High Li-ion conductive composite polymer electrolytes for all-solid-state Li-metal batteries. *J. Power Sources* **2021**, *482*, 228929.

(20) Yan, G.; Yu, S.; Nonemacher, J. F.; Tempel, H.; Kungl, H.; Malzbender, J.; Eichel, R.-A.; Krüger, M. Influence of sintering temperature on conductivity and mechanical behavior of the solid electrolyte LATP. *Ceram. Int.* **2019**, *45*, 14697-14703.

(21) Xu, Q.; Tsai, C.-L.; Song, D.; Basak, S.; Kungl, H.; Tempel, H.; Hausen, F.; Yu, S.; Eichel, R.-A. Insights into the reactive sintering and separated specific grain/grain boundary conductivities of $Li_{1.3}Al_{0.3}Ti_{1.7}(PO_4)_3$. *J. Power Sources* **2021**, *492*, 229631.

(22) Banerjee, A.; Wang, X.; Fang, C.; Wu, E. A.; Meng, Y. S. Interfaces and Interphases in All-Solid-State Batteries with Inorganic Solid Electrolytes. *Chem. Rev.* **2020**, *120*, 6878-6933.

(23) Nie, K.; Hong, Y.; Qiu, J.; Li, Q.; Yu, X.; Li, H.; Chen, L. Interfaces Between Cathode and Electrolyte in Solid State Lithium Batteries: Challenges and Perspectives. *Front. Chem.* **2018**, *6*, 616.

(24) Asl, N. M.; Keith, J.; Lim, C.; Zhu, L.; Kim, Y. Inorganic solid/organic liquid hybrid electrolyte for use in Li-ion battery. *Electrochim. Acta* **2012**, *79*, 8-16.

(25) Song, S.; Qin, X.; Ruan, Y.; Li, W.; Xu, Y.; Zhang, D.; Thokchom, J. Enhanced performance of solid-state lithium-air batteries with continuous 3D garnet network added composite polymer electrolyte. *J. of Power Sources* **2020**, *461*, 228146.

(26) Zhao, Y.; Ding, Y.; Li, Y.; Peng, L.; Byon, H. R.; Goodenough, J. B.; Yu, G. A chemistry and material perspective on lithium redox flow batteries towards high-density electrical energy storage. *Chem. Soc. Rev.* **2015**, *44*, 7968-7996.

(27) Fu, K.; Gong, Y.; Hitz, G. T.; McOwen, D. W.; Li, Y.; Xu, S.; Wen, Y.; Zhang, L.; Wang, C.; Pastel, G.; Dai, J.; Liu, B.; Xie, H.; Yao, Y.; Wachsman, E. D.; Hu, L. Three-dimensional bilayer garnet solid electrolyte based high energy density lithium metal–sulfur batteries. *Energy Environ. Sci.* **2017**, *10*, 1568-1575.

(28) Weiss, M.; Simon, F. J.; Busche, M. R.; Nakamura, T.; Schröder, D.; Richter, F.

H.; Janek, J. From Liquid- to Solid-State Batteries: Ion Transfer Kinetics of Heteroionic Interfaces. *Electro. ener. rev.* **2020**, *3*, 221-238.

(29) Li, J.; Zhu, K.; Wang, J.; Yan, K.; Liu, J.; Yao, Z.; Xu, Y. Optimisation of conductivity of PEO/PVDF-based solid polymer electrolytes in all-solid-state Li-ion batteries. *Mater. Technol.* **2020,** 1-8.

(30) Zha, W.; Li, W.; Ruan, Y.; Wang, J.; Wen, Z. In situ fabricated ceramic/polymer hybrid electrolyte with vertically aligned structure for solid-state lithium batteries. *Energy Storage Mater.* **2021**, *36*, 171-178.

(31) Tang, J.; Wang, L.; You, L.; Chen, X.; Huang, T.; Zhou, L.; Geng, Z.; Yu, A. Effect of Organic Electrolyte on the Performance of Solid Electrolyte for Solid-Liquid Hybrid Lithium Batteries. *ACS Appl. Mater. Interfaces* **2021**, *13*, 2685-2693.

(32) He, S.; Xu, Y. Hydrothermal-assisted solid-state reaction synthesis of high ionic conductivity $Li_{1+x}Al_xTi_{2-x}(PO_4)_3$ ceramic solid electrolytes: The effect of Al^{3+} doping content. *Solid State Ionics* **2019**, *343*, 115078.

(33) Pogosova, M.; Krasnikova, I.; Sergeev, A.; Zhugayevych, A.; Stevenson, K. Correlating structure and transport properties in pristine and environmentally-aged superionic conductors based on $Li_{1.3}Al_{0.3}Ti_{1.7}(PO_4)_3$ ceramics. *J. Power Sources*, **2020**, *448*, 227367.

(34) Srivastava, N.; Singh, S. K.; Gupta, H.; Meghnani, D.; Mishra, R.; Tiwari, R. K.; Patel, A.; Tiwari, A.; Singh, R. K. Electrochemical performance of Li-rich NMC cathode material using ionic liquid based blend polymer electrolyte for rechargeable

Li-ion batteries. *J. Alloys Compd.* **2020**, *843*, 155615.

(35) Celik, M.; Kızılaslan, A.; Can, M.; Cetinkaya, T.; Akbulut, H. Electrochemical investigation of PVDF: HFP gel polymer electrolytes for quasi-solid-state Li-O$_2$ batteries: effect of lithium salt type and concentration. *Electrochim. Acta* **2021**, *371*, 137824.

(36) Zhu, Y.; He, X.; Mo, Y. Origin of Outstanding Stability in the Lithium Solid Electrolyte Materials: Insights from Thermodynamic Analyses Based on First-Principles Calculations. *ACS Appl. Mater. Interfaces* **2015**, *7*, 23685−23693.

(37) Liu, D.; Qian, K.; He, Y.-B.; Luo, D.; Li, H.; Wu, M.; Kang, F.; Li, B. Positive film-forming effect of fluoroethylene carbonate (FEC) on high-voltage cycling with three-electrode LiCoO2/Graphite pouch cell. *Electrochim. Acta* **2018**, *269*, 378-387.

(38) Jin, Y.; Liu, C.; Zong, X.; Li, D.; Fu, M.; Tan, S.; Xiong, Y.; Wei, J. Interface engineering of Li$_{1.3}$Al$_{0.3}$Ti$_{1.7}$(PO$_4$)$_3$ ceramic electrolyte via multifunctional interfacial layer for all-solid-state lithium batteries. *J. Power Sources* **2020**, *460*, 228125.

(39) Yoshinari, T.; Koerver, R.; Hofmann, P.; Uchimoto, Y.; Zeier, W. G.; Janek, J. Interfacial Stability of Phosphate-NASICON Solid Electrolytes in Ni-Rich NCM Cathode-Based Solid-State Batteries. *ACS Appl. Mater. Interfaces*, **2019**, *11*, 23244-23253.

(40) Zhang, W.; Weber, D. A.; Weigand, H.; Arlt, T.; Manke, I.; Schroder, D.; Koerver, R.; Leichtweiss, T.; Hartmann, P.; Zeier, W. G.; Janek, J. Interfacial Processes and Influence of Composite Cathode Microstructure Controlling the Performance of All-Solid-State Lithium Batteries. *ACS Appl. Mater. Interfaces*, **2017**, *9*, 17835-17845.

Table of Contents.